# Magnetic Anisotropy Energy of Transition Metal Alloy Clusters

**Nabil M.R. Hoque, Tunna Baruah, J. Ulises Reveles and Rajendra R. Zope**

**Abstract** The binary clusters of transition metal atoms form an interesting platform for studying the effects of shape, size, chemical compositions, and ordering on its magnetic properties. Notably, mixed clusters often show higher magnetic moments compared to pure elemental clusters. Due to the reduced dimension of the clusters, they tend to behave as single domain particles. One important parameter of their magnetic behavior is the magnetic anisotropy energy. In this chapter we review previous works on the magnetic anisotropy energy of binary alloy clusters, along with a density functional theory based method to compute the anisotropy energy with applications to binary metal clusters. The clusters of transition metal atoms often show high spin moments but generally are also reactive with the environment. Passivation of the surface atoms can lead to more stable clusters. We have explored one such avenue for passivation in this work. We consider the $As@Ni_{12}@As_{20}$ cluster which in the neutral state has a magnetic moment of 3 $\mu_B$. We dope this cluster by substituting various numbers of Ni atoms by Mn atoms. The substitutional doping leads to spin moments located mostly on the Mn atoms. The doping also leads to symmetry breaking and as a consequence the number of structural isomers and spin ordered states for each isomer becomes very large. We have investigated all possible ferromagnetic isomers for a given number of dopants and subsequently all the possible anti-ferromagnetic states for the lowest energy structure were examined. The results show that the encapsulation within the $As_{20}$ cage stabilizes the clusters and the atomization energy of the clusters increases as the number of dopant increases. These clusters have small energy barrier for reversal of magnetization and also have rich variation in configuration and spin states with many low-lying spin states.

N.M.R. Hoque · T. Baruah · J. Ulises Reveles · R.R. Zope (✉)
Department of Physics, University of Texas El Paso, El Paso, TX 79968, USA
e-mail: rzope@utep.edu

J. Ulises Reveles
Department of Physics, Virginia Commonwealth University, Richmond, VA 23284, USA



M.T. Nguyen and B. Kiran (eds.), *Clusters*, Challenges and Advances in Computational Chemistry and Physics 23,
DOI 10.1007/978-3-319-48918-6_8

## 1 Introduction

The atomic clusters of transition metals (TM) have been studied extensively over the last three decades. The main interest in the transition metal clusters arises from their magnetic and catalytic properties. The super-paramagnetic behavior of magnetic nanoparticles has been known since mid-twentieth century [1]. Magnetic nanoparticles have been used for recording purposes and are also being experimentally used for medical purposes where their magnetic properties are exploited for drug delivery or for bio-imaging. More novel applications of the magnetic particles may emerge in future.

The nanoparticles used in data storage or for biomedical engineering are typically large extending from tens to hundreds of nanometers [2, 3]. The atomic clusters containing tens of atoms on the other hand fall in the small size regime of the nanoparticles [4]. The atomic clusters in this range often show very different properties from the bulk materials [5]. The reduction in size results in larger variation in coordination numbers (compared to bulk) that usually leads to structures significantly different from bulk fragments. As the cluster size grows the structure starts to resemble bulk fragments. However, even for larger clusters, significant fraction of the atoms are still on the surface and are under coordinated which leads to interesting chemical properties [5]. For example, the TM clusters are also used to attach and transport other molecules to targeted areas in biomedicine [2].

The transition metal clusters typically have non-zero spin moment [5–12]. Clusters smaller in size than the typical bulk magnetic domains behave as single magnets. The spin-orbit interaction leads to the magneto crystalline anisotropy that results in an energy barrier in flipping the direction of the spin. As the cluster size increases the magnetic anisotropy energy (MAE) decreases and can become comparable to thermal energy for large particles. Such large particles ($\sim$10 nm) can undergo super-paramagnetic relaxation. The super-paramagnetic behavior of the clusters is exploited in applications as contrasting agent whereas for the data storage purposes an energy barrier between the magnetic states higher than the ambient temperature is highly desirable. For a cluster to possess higher energy barrier it needs to have a large spin moment. It is to be noted that a large value of spin moment does not necessarily result in higher anisotropy barrier. It is found that the alloy clusters often have larger magnetic moment compared to clusters of one element. For example, in mixed Co–Rh clusters the Rh atoms are found to have induced spin moments [13]. The alloying offers the possibility of achieving a high variability in composition and structure, which in turn govern the electronic properties.

In this chapter, we focus on the discussion of anisotropy energy barrier in the transition metal alloy clusters. The metal clusters are typically more reactive due to under coordinated surface atoms. Passivation of the clusters can saturate the bonds and make the cluster chemically stable. Another way is to encapsulate the metal clusters in an inorganic cage to stabilize these clusters. This chapter provides a brief review of earlier work done on magnetic anisotropy in bare TM alloy clusters with a discussion of recent work on encapsulated TM clusters.

## 2 Magnetic Anisotropy in Transition-Metal Alloy Clusters

The transition metal alloy clusters have been studied both theoretically and experimentally for their magnetic and chemical properties [14–29]. Enhancing a particular property through dopants is an effective way in materials science to investigate new species with potential applications [25, 30–33]. The vast variability of size, structure and stoichiometry in clusters requires detailed systematic study. In this work we consider only bimetallic alloy clusters. The alloy clusters can form mixtures or segregated clusters mostly due to their different sizes [34]. The mixing pattern in such clusters was classified by Johnston et al. as core-shell, mixed, subcluster segregated, and multi-shell [4]. The magnetic properties of a few types of mixed clusters have been studied experimentally. A large number of early theoretical calculations mainly focused on the spin alignment in the clusters. Early on it was noted from theoretical calculations that the mixed 3d metal clusters have higher spin moments than the elemental clusters [35]. It was found that embedding clusters of 3d transition metal (Fe) in a non-magnetic solid (Ag) can lead to giant magneto resistance [36]. This interesting experimental result led to many works on alloy clusters of 3d transition metal atoms with 4d or 5d metal atoms. The 3d materials have high spin moment and the 4d materials show strong spin-orbit coupling. When combined these two effects can lead to systems with high magnetic anisotropy energy. Moreover, enhancement of the spin moments on the 4d/5d atoms also leads to higher magnetic moment of the cluster. One such system is Pd coated Ni nanoparticles which were found to possess a ferromagnetic Ni core surrounded by ferromagnetic and paramagnetic Pd layer. However, the magnetization showed steep saturation in hydrogen atmosphere [37]. On the other hand, intermixed Ni–Pd alloy nanoparticles were found to be superparamagnetic with a blocking temperature of 290 K [38]. Co–Rh alloy particles have shown strong enhancement of magnetization compared to bulk alloys. This effect is attributed to a combination of size reduction and coupling with a magnetic 3d element (Co), leading to an enhanced induced electronic spin polarization of the 4d (Rh) atoms, while retaining the magnetism due to the Co atoms [39–41]. In these clusters there is an induced magnetic moment on the Rh atoms with increasing Co concentration, which results in an increase in the average magnetic moment per atom. Rohart et al. studied the magnetic anisotropy energy of Co–Pt mixed clusters embedded in various matrix [19, 42]. By comparing different chemical compositions they found that a small amount of Pt induces increase in volume anisotropy. Tournus et al. have noted the dispersion of the anisotropy constant in size selected CoPt alloy clusters which shows the chemical environment of the Co atoms is important as it directly determines the anisotropy. Luis et al. [42] have reported significant increase in blocking temperature and coercive field for Co clusters capped by a thin Au layer [20]. Detailed theoretical studies have been done on the magnetic anisotropy energy (MAE) of mixed clusters of Co–Rh [13, 43, 44] CoPd [41, 45], Pt covered Co, Fe

and Ni clusters [46], Fe–Co mixed clusters [28], Co–Mo mixed clusters [47]. Theoretical works point out the contribution from the orbital magnetic moment, and also the importance of chemical composition or environment of the 3d metal atoms. The mixed clusters with 4d or 4d non-magnetic atoms showed enhanced spin moment on the 4d or 5d atoms. The Pt covered Co clusters retained the magnetization properties of the Co cluster in core-shell structure but increased the volume anisotropy in case of mixed clusters. On the other hand, Au capped Co clusters showed enhanced magnetization. From these studies it is evident that alloying helps in enhancement of magnetization but also depends on the structure. Materials assembled from such clusters have vast potential for novel applications but more studies are needed. In the following we describe a density functional based method for calculation of the magnetic anisotropy energy in molecules and clusters followed by some recent applications to mixed TM clusters.

## 3 Magnetic Anisotropy Energy

Magnetic materials are said to have magneto crystalline anisotropy if it takes a stronger field to magnetize in a specific direction compared to the others. Depending on the orientation of the field with respect to the crystal lattice one would need a lower or higher magnetic field to reach magnetic saturation, a characteristic that leads to the definition of two types of axes, the easy and the hard one, that arise from the interaction of the spin magnetic moment with the crystal lattice. The easy axis is the direction inside a crystal, along which a small applied magnetic field, is sufficient to reach the magnetic saturation. Finally, the magneto-crystalline anisotropy energy is the energy needed to deflect the magnetic moment in a single crystal from the easy to the hard direction.

The magnetic anisotropy energy barrier is related to the zero-field splitting of the spin states due to spin-orbit coupling. A few algorithms have been formulated to compute magnetic anisotropy within density functional theory [48, 49]. The discussion below follows an approach due to Pederson and Khanna [48], Pederson and Baruah [50]. In the classical explanation of spin-orbit coupling an electron moving with velocity **v** and accounting for the fact that electron is not spinless, the interaction energy is given by,

$$U(\boldsymbol{r},\boldsymbol{p},\boldsymbol{S}) = -\frac{1}{2c^2}\boldsymbol{S}.\boldsymbol{p} \times \nabla\varphi(\boldsymbol{r}), \tag{1}$$

where $\boldsymbol{\varphi}(\boldsymbol{r})$ is the Coulomb potential, $\boldsymbol{p}$ is the momentum operator. The determination of spin-orbit coupling matrix element is a necessary ingredient to the numerical solution of the Schrodinger equation. To determine the generalized spin-orbit interaction from Eq. (1) it is necessary to calculate matrix element of the form,

$$\begin{aligned} U_{j,\sigma,k,\sigma'} &= \langle f_j \chi_\sigma | U(\boldsymbol{r},\boldsymbol{p},\boldsymbol{S}) | f_k \chi_{\sigma'} \rangle \\ &= \sum\nolimits_x \frac{-1}{i2c^2} \langle f_j | [\nabla \times \nabla \varphi(\boldsymbol{r})]_x | f_k \rangle \langle \chi_\sigma | S_x | \chi_{\sigma'} \rangle \\ &= \sum\nolimits_x \frac{1}{i} \langle f_j | V_x | f_k \rangle \langle \chi_\sigma | S_x | \chi_{\sigma'} \rangle, \end{aligned}$$

with the operator $V_x$ defined according to

$$\langle f_j | V_x | f_k \rangle = \frac{-1}{2c^2} \left\langle f_j \left| \frac{d}{dy}\frac{d\varphi}{dz} - \frac{d}{dz}\frac{d\varphi}{dy} \right| f_k \right\rangle. \tag{2}$$

Using the identity,

$$\left\langle f_i \frac{d\varphi}{dy}\frac{d}{dz} f_j \right\rangle = \int d^3 r \frac{d}{dy}\left[ f_i \varphi \frac{df_j}{dz} \right] - \left\langle \frac{df_i}{dy} | \varphi | \frac{df_j}{dz} \right\rangle - \left\langle f_i | \varphi | \frac{d^2 f_j}{dz dy} \right\rangle,$$

we get

$$\langle f_j | V_x | f_k \rangle = \frac{1}{2c^2} \left( \left\langle \frac{df_j}{dz} | \varphi | \frac{df_k}{dy} \right\rangle - \left\langle \frac{df_j}{dy} | \varphi | \frac{df_k}{dz} \right\rangle \right). \tag{3}$$

The matrix elements for $V_y$ and $V_z$ are determined by the cyclic permutation.

Let us assume that, in the absence of a magnetic field and spin-orbit coupling, we have determined the wave functions $\psi_{i\sigma}$ within a self-consistent field (SCF) approximation. The SCF wave functions satisfy

$$H|\psi_{i\sigma}\rangle = \epsilon_{i\sigma}|\psi_{i\sigma}\rangle,$$

where $|\psi_{i\sigma}\rangle$ is a product of a spatial function and spinor according to $|\psi_{i\sigma}\rangle = \varphi_{i\sigma}(\boldsymbol{r})\chi_\sigma$.

With the inclusion of spin-orbit coupling and the introduction of a magnetic of field the perturbed wave functions satisfy,

$$\left[ H + \left( \frac{V}{i} + \frac{1}{c}\boldsymbol{B} \right) \cdot \boldsymbol{S} \right] \psi'_{i\sigma}\rangle = \epsilon'_{i\sigma} |\psi'_{i\sigma}\rangle.$$

Here, the operator $\boldsymbol{V}$ is defined according to Eq. (3) and the magnetic field ($\mathbf{B}$) is assumed to be uniform.

Now let $\boldsymbol{W} = \left(\frac{V}{i} + \frac{1}{c}\boldsymbol{B}\right)$. According to the second order perturbation theory, the Hamiltonian matrix is perturbed by the following equation,

$$\Delta = \Delta_1 + \Delta_2.$$

In the absence of applied magnetic field the first order energy shift is,

$$\Delta_1 = \sum_{i\sigma} S_i^{\sigma\sigma} \sum_k \langle \varphi_{k\sigma} | W_i | \varphi_{k\sigma} \rangle.$$

The first order energy shift vanishes due to the operator $-i\boldsymbol{V}\cdot\boldsymbol{S}$ and the first order correction to the orbital is purely imaginary. The second order energy shift is,

$$\Delta_2 = \sum_{i\sigma'} \sum_{ij} W_{ij}^{\sigma\sigma'} S_i^{\sigma\sigma'} S_j^{\sigma'\sigma}, \tag{4}$$

where, $S_i^{\sigma\sigma\prime} = \langle \chi_\sigma | S_i | \chi_{\sigma'}^{'} \rangle$,
and, $W_{ij}^{\sigma\sigma'} = W_{ji}^{\sigma\sigma'*} = \sum_{ij} \frac{\langle \varphi_{k\sigma} | W_i | \varphi_{l\sigma'} \rangle \langle \varphi_{k\sigma'} | W_j | \varphi_{l\sigma} \rangle}{\epsilon_{k\sigma} - \epsilon_{l\sigma'}}$ .

In Eq. 4 here the 1st sum is running over spin-up and spin-down states. In the 2nd sum we are running over all the co-ordinate levels (x, y, z). The $W$ matrices are simplified to,

$$W_{ij}^{\sigma\sigma'} = -\sum_{kl} \frac{\langle \sigma_{k\sigma} | V_i | \sigma_{l\sigma'} \rangle \langle \sigma_{l\sigma'} | V_j | \sigma_{k\sigma} \rangle}{\epsilon_{k\sigma} - \epsilon_{l\sigma'}} + \frac{B_i B_j}{c^2} \sum_{kl} \frac{< \sigma_{k\sigma} | V_i | \sigma_{l\sigma'} \rangle \langle \sigma_{l\sigma'} | V_j | \sigma_{k\sigma} \rangle}{\epsilon_{k\sigma} - \epsilon_{l\sigma'}}$$

In the limit of B approaching zero, the second term vanishes and the W matrix becomes as follows

$$W_{ij}^{\sigma\sigma'} \rightarrow M_{ij}^{\sigma\sigma'} = -\sum_{kl} \frac{< \sigma_{k\sigma} | V_i | \sigma_{l\sigma'} > < \sigma_{l\sigma'} | V_j | \sigma_{k\sigma} >}{\epsilon_{k\sigma} - \epsilon_{l\sigma'}}. \tag{5}$$

In the above equations $\chi_\sigma$ and $\chi'_\sigma$ are any set of spinors.$\varphi_{k\sigma}$ and $\varphi_{l\sigma'}$ are the occupied and unoccupied states respectively. $\epsilon's$ are the corresponding energies.

The second-order shift in the energy of the system in the absence of a magnetic field can be rewritten as, $\Delta_2 = \sum_{ij} \gamma_{ij} \langle S_i \rangle \langle S_j \rangle$. By diagonalizing the anisotropy tensor $(\gamma)$, the anisotropy energy can be determined. The value of $\gamma$ can be calculated within the density functional framework using second-order perturbation theory and in terms of Kohn-Sham orbitals, it is given by,

$$\gamma = \left( \frac{2}{\Delta N^2} \right) \left( M_{zz}^{11} + M_{zz}^{22} + M_{xx}^{12} + M_{xx}^{21} - M_{xx}^{11} - M_{xx}^{22} - M_{zz}^{12} - M_{zz}^{21} \right),$$

*w*here ΔN is the number of unpaired electrons. Once the anisotropy tensor is diagonalized the second-order energy shift can be rewritten as,

$$\Delta_2 = \frac{1}{3}\left(\gamma_{xx}+\gamma_{yy}+\gamma_{zz}\right)S(S+1) + \frac{1}{3}\left[\gamma_{zz} - \frac{1}{2}\left(\gamma_{xx}+\gamma_{yy}\right)\right] \times \left[3S_z^2 - S(S+1)\right] + \frac{1}{2}(\gamma_{xx}-\gamma_{yy})(S_x^2 - S_y^2). \tag{6}$$

The anisotropy Hamiltonian splits the 2S + 1 spin states and when the isotropi term is ignored, it can be expressed as

$$H = DS_z^2 + E\left(S_x^2 - S_y^2\right), \tag{7}$$

The value of D and E parameters in the above equation can be directly obtained from the $\gamma_{xx}$, $\gamma_{yy}$, $\gamma_{zz}$ and therefore the magnetic anisotropy energy can be obtained.

The method described above is implemented in the NRLMOL suite of software [51–56]. Below we present results of previous calculations on several single molecule magnets and compare them with experimental values for benchmark purpose.

The values of the axial anisotropy parameter D in Eq. 7 are available from a number of experiments for different single molecule magnets (SMM). Several first-principle calculations have been carried out with the use of the NRLMOL code on SMMs such as $Mn_{12}$ [48, 57, 58], $Mn_{10}$ [59], Ferric star, $Fe_4$, $Fe_8$ [60–62], $Mn_4$ [63], $Co_4$ [64], $Mn_9$ [65] etc. These results are summarized in Table 1. In general a good agreement of the spin ordering is found between theoretical calculations and experiments. The broken symmetry approach is needed for systems with antiferromagnetic spin ordering. Moreover, the calculated D parameters for $Mn_{12}$, $Mn_{10}$, $Mn_9$, the ferric star $Fe_4$ and Cr-amide molecular magnets are in excellent agreement with experimental values. The only discrepancy is found for $Fe_8$, a system that seems to pose complications for the DFT treatment. Apparently DFT may be unable to predict the ground state density accurately enough due to important electronic correlations beyond the mean-field treatment or missing Madelung stabilization

**Table 1** Comparison of experimental and NRLMOL calculated magnetic anisotropy parameters (D)

| Molecule | S | MAE (K) | |
|---|---|---|---|
| | | Experiment | Theory |
| $Mn_{12}O_{12}(O_2CH)_{16}(H_2O)_4$ | 10 | −0.56 | −0.56 [48] |
| $[Fe_8O_2(OH)_{12}(C_6H_{15}N_3)_6Br_6]^{2+}$ | 10 | −0.30 | −0.53 [60] |
| $[Mn_{10}O_4(2,2'\text{-biphenoxide})_4Br_{12}]^{4-}$ | 13 | −0.05 | −0.06 [59] |
| $Co_4(CH_2C_5H_4N)_4(CH_3OH)_4Acl_4$ | 6 | −0.7 to −0.09 | −0.64 [66] |
| $Fe_4(OCH_2)_6(C_4H_9ON)_6$ | 5 | −0.57 | −0.56 [67] |
| $Cr[N(Si(CH_3)_3)_2]_3$ | 3/2 | 2.66 | −1.15 [67] |
| $Mn_9O_{34}C_{32}N_3H_{35}$ | 17/2 | −0.32 [65] | −0.33 [65] |
| $Mn_4O_3Cl_4(O_2CCH_2CH_3)_3(NC_5H_5)_3$ | 9/2 | −0.72 | −0.58 [63] |

(absent in the isolated system). The SMMs listed in Table 1 are in general characterized by a high spin ground-state. However, a high spin state does not necessarily correlate with a high anisotropy barrier. The parameter D is also very important. In order to increase the barrier one has to understand and control D, which will be the main goal of future research in this area. In all cases where the E parameter is not zero by symmetry it has been predicted with similar accuracy as D. These results provide confidence in the predictive ability of the formalism.

## 4 Applications to Transition Metal Mixed Clusters

### (a) $Fe_nCo_m$Clusters:

Kortus et al. used NRLMOL to study $Fe_nCo_m$ ($n + m = 5$ and 13) binary clusters with bipiramidal and icosahedral symmetries shown in Fig. 1, and investigated the effects of alloying on its magnetic moment and MAEs [28]. The dopant atoms were placed along the molecular axis. Their density-functional study showed that many alloy clusters have moments comparable to or higher than those present in pure clusters of Fe or Co, ranging from 13 to 41 $\mu_B$. They found these systems have very low anisotropies, 1.8 to −63 K (Cf. Table 2) making them ideal candidates for soft magnetic materials. The bulk Co has higher anisotropy than pure Fe or mixed Fe–Co alloys however the Co clusters have the lowest anisotropy. This work showed that a high magnetic anisotropy requires a strong coupling between occupied and unoccupied states close to the Fermi energy, and that one possible way to accomplish this may be by generating unreactive, compositionally ordered uniaxial clusters with small gaps. It also highlights the importance of shape, composition and compositional ordering in mixed atom clusters.

### (b) $Co_nMo_m$NANOCLUSTERS

Cobalt dimer has a large magnetic anisotropy [68–71]. Garcia-Fuente et al. studied $Mo_{4-x}$ $Fe_x$ and concluded that these clusters are good candidates for molecular electronic devices [72]. It has also been shown that $Mo_2X_2$ (X = Fe, Co, Ni) clusters are able to act as spin filters [73]. These observation led Liebing et al. to

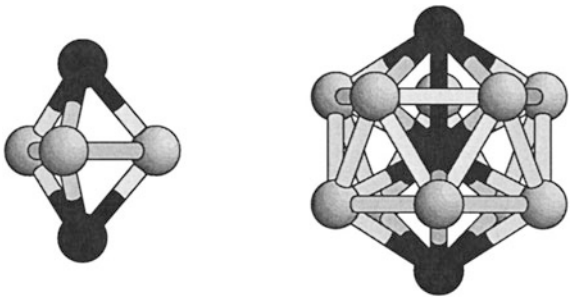

**Fig. 1** The uniaxial geometrical configurations for the 5 and 13 atoms cluster, triangular bipyramid geometries and distorted icosahedrons. The dopant atoms were placed along the uniaxial axis. Reprinted with permission from [28]. Copyright 2002, AIP Publishing LLC

**Table 2** Magnetic moment and MAE for the relaxed 5-atom and 13-atom clusters

| Cluster | Moment ($\mu_B$) | MAE (K) |
|---|---|---|
| $Co_5$[a] | 13 | 6 |
| $Co_3Fe_2$ | 13 | 27/15 |
| $Co_2Fe_3$ | 16 | 21 |
| $Fe_5$ | 16 | 14 |
| $Co_{13}$ | 21 | 0 |
| $Co_{10}Fe_3$ | 30 | 63 |
| $Fe_{10}Co_3$ | 41 | 9 |
| $Fe_{13}$ | 44 | 41 |

[a]Reprinted with permission from [28]. Copyright 2002, AIP Publishing LLC

**Table 3** Magnetic ground state S and magnetic anisotropy energy MAE for the $Co_nMo_m$ clusters

| Cluster | S | MAE (K) | Cluster | S | MAE (K) |
|---|---|---|---|---|---|
| $Co_2$ | 2 | −5.6 | $Co_4Mo$ | 4 | −1.5 |
| CoMo | 3/2 | 13.4 | $Co_3Mo_2$ | 5/2 | −1.6 |
| $Co_3$ | 5/2 | −6.5 | $Co_2Mo_3$ | 2 | 6.1 |
| $Co_2Mo$ | 2 | 12.5 | $Co_6$ | 7 | −0.02 |
| $Co_4$ | 5 | 1.0 | $Co_5Mo$ | 9/2 | −0.6 |
| $Co_3Mo$ | 5/2 | 10.7 | $Co_4Mo_2$ | 3 | −2.7 |
| $Co_2Mo_2$ | 2 | −5.9 | $Co_3Mo_3$ | 5/2 | 3.6 |
| $CoMo_3$ | 3/2 | 8.5 | $Co_2Mo_4$ | 2 | −10.8 |
| $Co_5$ | 11/2 | −1.2 | – | – | – |

Reprinted Table with permission from [47]. Copyright 2015 by the American Physical Society

investigate $Co_nMo_m$ nanoclusters [47] with $n + m = x$ and $2 <= \times <= 6$. They studied pure cobalt and molybdenum clusters and compared their properties with those of its respective mixed species for each cluster size $x$. They found that the magnetic moment of a given cluster is mainly determined by the Co content and increases with increasing $n$. The magnetic anisotropy on the other hand becomes smaller for larger magnetic moments as shown in Table 3. They reported the variation of the electronic properties of the clusters as a function of size. An increase in binding energy, electron affinity, and average bond length, and a decrease in ionization potential, chemical potential, molecular hardness, and the HOMO–LUMO gap was found for increasing cluster size.

(c) Encapsulated Clusters

Cluster based materials offer the potential for new novel properties, which can be tuned by changing the cluster structure, composition, size, coordinating ligands etc. One of the reasons that gas phase metal cluster properties cannot be interpreted as indicator of the cluster based bulk materials is that the clusters often have unsaturated bonds and therefore are chemically active. Such gas-phase clusters may

change their size and properties when in a bulk environment. However, these clusters could be protected using organic/inorganic ligands. One such example is the $[As@Ni_{12}@As_{20}]^{3-}$ ion that was isolated in 2004 by Eichhorn and coworkers [74]. This ion has perfect icosahedral symmetry and has a structure that contains an icosahedral $Ni_{12}$ cluster embedded in the dodecahedral $As_{20}$ cage. The inner icosahedral $Ni_{12}$ cluster has an arsenic atom at its center. The two interlocked cages result in a polyhedron containing 60 triangular faces with icosahedral symmetry. Subsequent density functional calculations showed that the bonding between the $As_{20}$ and $Ni_{12}@As$ units is about 26 eV and that the cluster was vibrationally stable in the gas phase [75, 76]. Recently, we carried out DFT calculations on the magnetic anisotropy energies of $As@Ni_{12}@As_{20}$ cluster doped with Mn atoms. The doping is substitutional in that the dopant Mn atoms replace Ni atoms in the cluster. The substitutional doping thus resulted in the $Ni_{12-x}Mn_x$ alloy clusters encapsulated within the $As_{20}$ cage. We doped the parent cluster by up to six Mn atom. Depending on the number of dopant Mn atoms, the substitutional doping can result in various isomers as there are multiple possible configurations of doping sites. We have considered all possible sites for substitutional doping. For every possible configuration of Mn dopants in the parent clusters, the lowest energy ferromagnetic isomer was obtained by geometry optimization. Subsequently, search for the lowest energy spin configuration was carried out by considering all possible ferrimagnetic isomers. We begin with the optimized geometry of the neutral $As@Ni_{12}@As_{20}$ cluster which we will henceforth refer to as the parent cluster. The geometrical parameters of the parent cluster optimized using the PBE functional were found to be in good agreement with experiment [76]. This cluster is highly symmetric with a magnetic moment of 3 μB. The high symmetry of the molecule rules out any anisotropy of magnetization. The $As@Ni_{12}@As_{20}$ cage is symmetric and as a result does not have any magnetic anisotropy. In this cage each Ni atom is coordinated with five As atoms. The Ni atoms form an icosahedral inner cage and thus each Ni atom is also coordinated to five other Ni atoms. The doping is substitutional in nature, that is, Ni atoms are replaced by the Mn atoms. As a result, the Mn atoms in these clusters also have similar coordination with As and Ni/other Mn atoms. The substitutional doping of the Ni atoms by multiple Mn atoms can result in various different isomers. We considered all possible substitutional ordering/permutations, that is, for a given x in $As@Ni_{12-x}Mn_x@As_{20}$ all possible isomers arising due to different configurations of substitutional doping were considered. The resultant geometry of every such an isomer was optimized simultaneously with spin optimization to find most stable isomers with ferromagnetic spin ordering. These results indicated that the spin charges are mainly located on the Mn atoms. Due to this reason, the search of possible ferrimagentic spin ordering involved spin orientations of only Mn atoms.

The calculations were carried out at the all-electron level using generalized gradient approximation of Perdew, Burke and Ernzerhof (PBE96) to describe the exchange-correlation effects [8]. The electronic orbitals and eigenstates are determined using a linear combination of Gaussian atomic type orbital molecular orbital (LCGTO) approach as implemented in the NRLMOL code developed by Pederson

and co-workers [9–11]. NRLMOL uses an optimized large basis set that include supplemental diffuse *d*-type polarization function [12]. The integrals are accurately and efficiently calculated using a variational mesh and an analytic solution of Poissons equation is implemented to accurately determine the self-consistent potentials, secular matrix, total energies, and Hellmann-Feynman-Pulay forces.

In the following we discuss the structural and electronic properties of each of the encapsulated alloy clusters in detail.

### $As@Ni_{11}Mn@As_{20}$

In the parent $As@Ni_{12}@As_{20}$ system, all Ni atoms that form inner icosahedron are equivalent by symmetry. Likewise, all the As atoms that form outer dodecahedral cage are also symmetrically equivalent. Since all Ni atoms are equivalent, one only needs to replace one of the 12 Ni atoms by Mn atom. Thus, there is only one resultant structure. The optimized structure of $As@Ni_{12}@As_{20}$ is shown in Fig. 2 below.

As evident from the figure, the $As_{20}$ cage in this case is distorted due to the expansion of the As–As bond lengths near Mn. The doping however leads to further stabilization of the cluster with a larger atomization energy of 4.93 eV compared to the 4.80 eV of the parent cluster. The gap between the highest occupied molecular orbital (HOMO) and the lowest unoccupied molecular orbital (LUMO) is 0.16 eV at the PBE level. The net spin moment in this molecule is $6\mu_B$. Our calculation on the charge density inside a sphere placed on the Mn shows that the spin charge on the Mn ion is 3.2 $\mu_B$. The spin moment on the Ni atoms are small within a range of 0.2 $\mu_B$. The presence of the Mn atom as well as the distortion of the cage breaks the symmetry of the system, resulting in second order MAE of 10.4 K. It forms a tri-axial system with a D parameter of 1.15 K and has E parameter of 0.06 K.

### $As@Ni_{10}Mn_2@As_{20}$

In the parent $As@Ni_{12}@As_{20}$ system, two Mn atoms were introduced by replacing two of the 12 Ni atoms. There are three unique resultant possible structures of the $As@Ni_{10}Mn_2@As_{20}$ which were first optimized in the ferromagnetic state. The

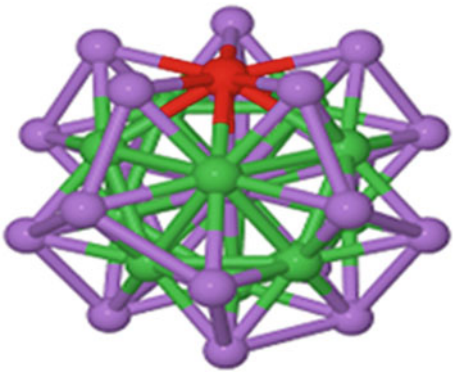

**Fig. 2** Structure of $As@Ni_{11}Mn@As_{20}$ cluster

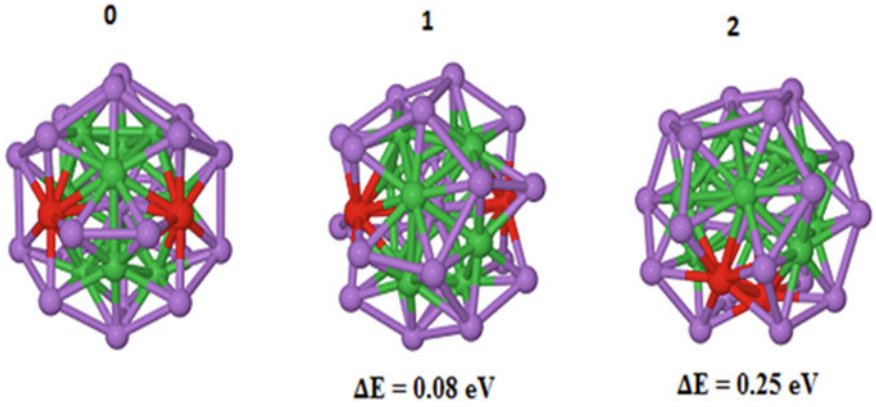


**Fig. 3** Three distinct isomers of $As@Ni_{10}Mn_2@As_{20}$

structures of the three ferromagnetic isomers are shown in Fig. 3. The lowest energy isomer has a net spin of 9 $\mu_B$ whereas the low-lying isomers both have spin moment of 7 $\mu_B$. The net spin on each of the Mn ions is 3.15 $\mu_B$ and the average spin on the Ni ions is 0.25 $\mu_B$, which in the ferromagnetic state leads to a net moment of 9 $\mu_B$ for the lowest energy structure. The lowest energy cluster has MAE on the order of 20 K. The cluster also has a gap of 0.25 eV, which indicates that the cluster is chemically more stable compared to the single Mn doped system.

The lowest ferromagnetic isomer was further optimized in an anti-ferromagnetic (AFM) state. The AFM spin configuration was achieved by applying a potential to force the spin orientation in the first iteration of the SCF cycle and later releasing it. Since there are only two Mn atoms in this cluster, only one antiferromagnetic ordering is possible. The antiferromagnetic spin ordering results in a structure that is higher in energy by 0.12 eV with a total magnetic moment of 1 $\mu_B$. We find that the Mn atoms induce similar spin orientation in the nearby Ni atoms.

### $As@Ni_9Mn_3@As_{20}$

The optimization of the three Mn doped $As_{21}Ni_{12}$ cage resulted in nine different isomers as shown in Fig. 3 below. All the isomers show distortion of the parent cluster from the highly symmetric structure due to alloying. There are a few low-lying isomers within 0.1 eV of the lowest energy structure. The magnetic moment in all clusters except isomer 7 is 12 $\mu_B$. The magnetic moment is 10 $\mu_B$ for this isomer in which all the three Mn ions are adjacent. Due to the breaking of symmetry of the parent cage, magnetic anisotropy energy becomes significant. The largest MAE is 37 K for the lowest energy ferromagnetic structure in which the distances between the Mn ions are 0.264, 0.536, 0.472 nm. The spin moments on the Mn atoms in this state are 3.1 $\mu_B$.

We have investigated various ferrimagnetic states of the lowest energy alloy cluster. There are three possible ferromagnetically ordered spin states and the cluster was optimized in all these states. We find one AFM state that is about

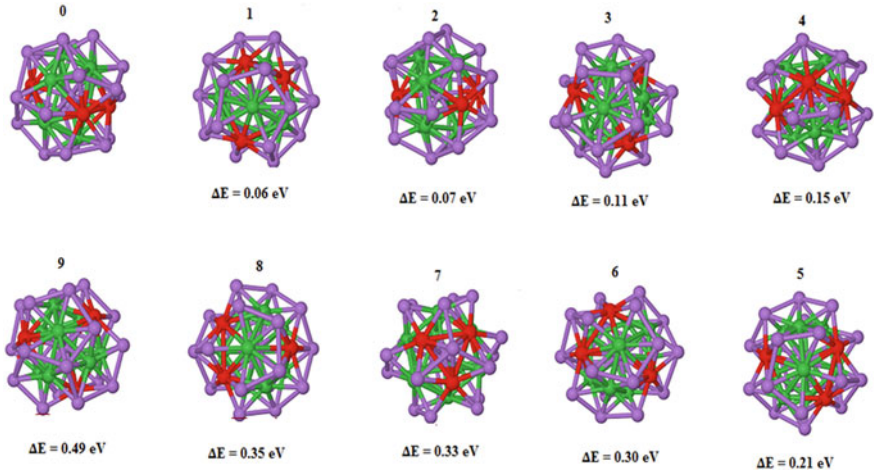


**Fig. 4** Isomers of $As@Ni_9Mn_3@As_{20}$

0.15 eV below the ferromagnetic state and forms the ground state of this isomer. This spin of this state is S = 2. The depiction of the anti-ferromagnetically ordered spin system is shown in Fig. 4. There is also another spin ordered state 0.05 eV above the lowest AFM state. The lowest energy AFM state shows an energy barrier of 18.6 K for reversal of magnetization. The three Mn doped system forms an easy axis with a D parameter of 4.5 K and an E parameter of 0.68 K. The corresponding parameters for the ferromagnetic state are 1.0 K and 0.1 K. The cluster undergoes structural changes in the AFM state in which the bonds with the nearest As atoms are shortened in two cases by as much as 0.11 Angstrom. The shortening of the bonds increases the crystal field as a result of which the D and E parameters are higher in the AFM state. However, due to the lower net spin of the cluster the overall MAE is lower for the AFM state (Fig. 5).

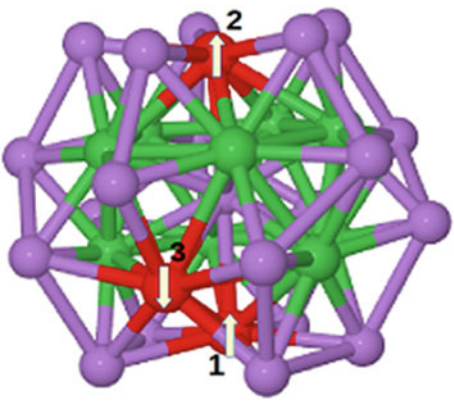


**Fig. 5** Spin ordering of Mn atom in $As@Ni_9Mn_3@As_{20}$

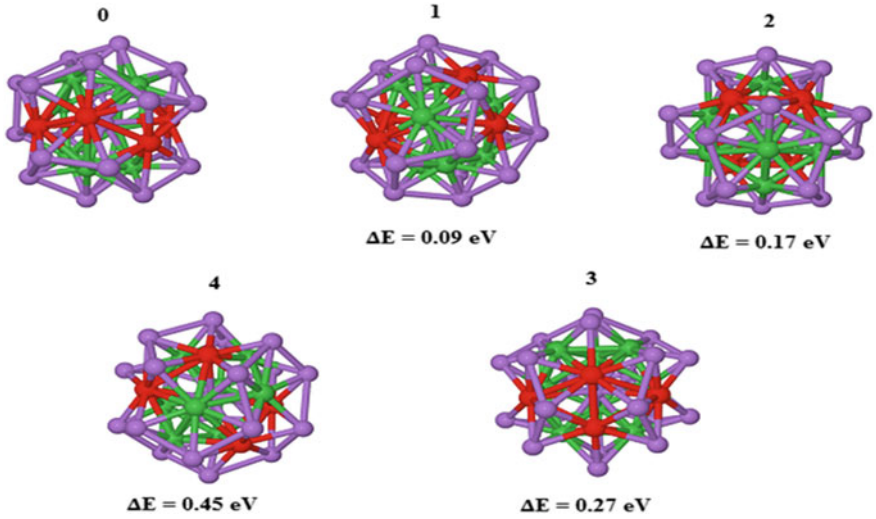


**Fig. 6** All the possible combination of $As@Ni_8Mn_4@As_{20}$ system

### $As@Ni_8Mn_4@As_{20}$

There are five possible unique structures which can be generated from $As@Ni_8Mn_4@As_{20}$ system by replacing four Ni atoms by Mn atoms. The optimized structures of $As@Ni_8Mn_4@As_{20}$ in the ferromagnetic state are shown in Fig. 6. The isomers are within a range of 0.09–0.45 eV above the lowest energy isomer. The spin magnetic moments in these isomers range from 13 to 15 $\mu_B$. The spin ordering is shown in Fig. 7. The local moments on the Mn atoms in the lowest FM isomer range from 2.4 to 3.1 $\mu_B$. The magnetic anisotropy energy in this cluster is 33 K. However, a study of the optimized spin-ordered clusters showed a ferromagnetic cluster with magnetic moment of 1 $\mu_B$ is found to be lower than the ferromagnetic cluster by 0.2 eV. The physical picture of the spin ordering is shown in Fig. 6.

### $As@Ni_7Mn_5@As_{20}$

We find seven stable isomers of the $As@Ni_7Mn_5@As_{20}$ clusters which were optimized first in the ferromagnetic state (Fig. 8). The lowest energy ferromagnetic structure has the five Mn atoms occupying adjacent positions in a pentagonal pyramid. The energies of the other isomers are within a range of 0.04–0.87 eV. We optimized all the possible spin ordered states of the lowest energy ferromagnetic (FM) isomer. In total, there are 12 such distinct ferrimagnetic states. We found one state which is lower in energy by only 0.03 eV compared to the FM state. There are two other AFM states within 0.03 eV from the lowest energy AFM state. Thus this cluster has several low-lying states, which differ in their structural as well as spin configuration. The HOMO–LUMO gap of the lowest energy AFM state is 0.32 eV,

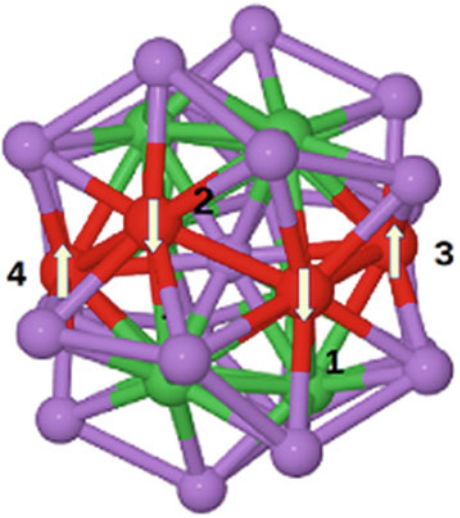


**Fig. 7** Spin ordering in the lowest energy structure of $As@Ni_8Mn_4@As_{20}$

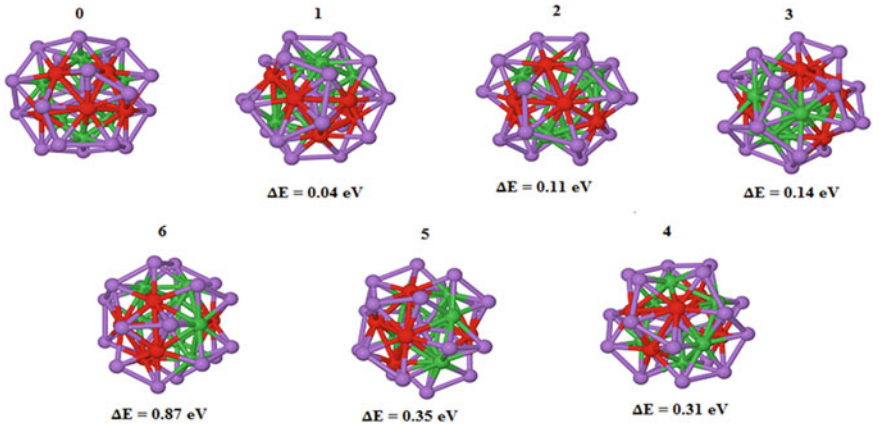


**Fig. 8** All the possible combination of $As@Ni_7Mn_5@As_{20}$ cluster according to their energy

which has spin moment 2 μB. The D and E parameters in the lowest energy AFM state are 6.4 and 4.7 K respectively. On the other hand, these parameters are much smaller in the FM state with values of 0.27 and 0.1 K for the D and E respectively (Fig. 9).

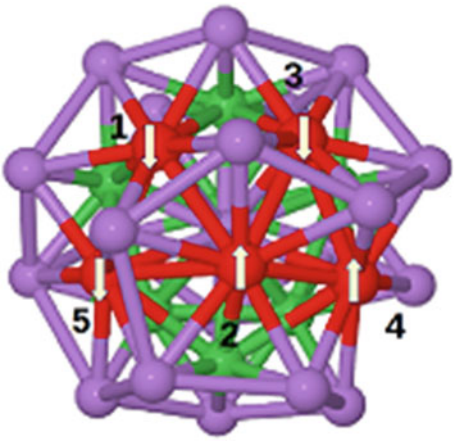


**Fig. 9** Spin ordering of Mn atoms in the lowest energy structure of $As@Ni_7Mn_5@As_{20}$ system

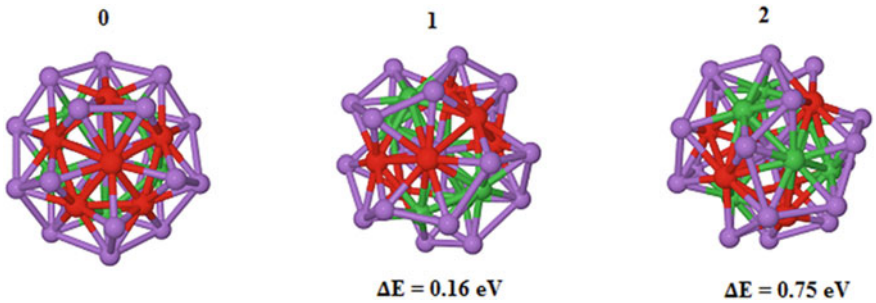


**Fig. 10** All the possible combination of $As@Ni_6Mn_6@As_{20}$ cluster according to their energy

### $As@Ni_6Mn_6@As_{20}$

In the parent $As@Ni_{12}@As_{20}$ system six Mn atoms are doped by replacing any six of the 12 Ni atoms. The optimized structures of ferromagnetic $As@Ni_6Mn_6@As_{20}$ isomers are shown in the Fig. 10.

The spin magnetic moment of these isomers varies from 15 to 21 $\mu_B$ in these clusters. The lowest structure has six Mn atoms forming a pentagonal pyramid. The MAE of the lowest energy isomer is 7 K. The binding energy of the six Mn doped cluster increases to 5.48 eV from 4.81 eV in the parent cluster. The gap of 0.25 eV suggests the cluster to be chemically stable. The presence of six Mn atoms in the cluster leads to 32 spin states in total. The most favorable ferromagnetic cluster is chosen for studying different spin ordering of the Mn atoms. To reduce the computational costs, the calculations on the anti-ferromagnetic states are first done as single point calculations. The lowest 10 spin ordered states of the cluster are selected and optimized in order to find the lowest energy spin-ordered clusters.

We find six AFM isomers that have lower energy compared to the ferromagnetic case. The energetically most favorable spin ordered cluster is shown in Fig. 11. This isomer has magnetic anisotropy energy barrier of 12.6 K. Similar to the other clusters studied here, the $As@Ni_6Mn_6@As_{20}$ cluster also has several closely spaced spin states with nearly same magnetic moments. It can be mentioned here that the bare $Mn_6$ cluster also has a ferrimagnetic spin arrangement but the preferred structure is octahedral with a magnetic moment of 9 $\mu_B$. Experimentally determined value of magnetic moment of the bare $Mn_6$ cluster ranges from 2 to 4 $\mu_B$ at temperature 50 K. The MAE of the bare $Mn_6$ cluster is 0 K compared to the 12 K of the $As@Mn_6Ni_6@As_{20}$ cluster. The spin moment on the individual Mn ions in $As@Ni_6Mn_6@As_{20}$ ranges from 2–3 $\mu_B$ compared to the 3.7 $\mu_B$ in the bare $Mn_6$ cluster. These comparisons show that the bonding of the Mn ions with the As and Ni atoms reduces the individual spin moments. Moreover, the chemical environment around the Mn atoms is important in the determination of the anisotropy energy.

The calculated results on the lowest energy FM and AFM states of the various doped $As@Ni_{12-x}Mn_x@As_{20}$ clusters are summarized in Table 4. We find that the doping by Mn distorts the geometry of the parent cluster but also increases the atomization energy of the whole cluster. The atomization energy of the parent $As@Ni_{12}@As_{20}$ cage is 4.8 eV which increases to 5.48 eV for the $As@Ni_6Mn_6@As_{20}$ cluster. The As–Mn bonds are shorter than the As–Ni bonds and the overall cluster size is reduced with the dopants. The lowest energy isomers have HOMO–LUMO gaps higher than 0.25 eV at the PBE level. The gaps also indicate higher chemical stability of the clusters. In general our study which included a large number of isomers indicated that the $Ni_{12-x}Mn_x$ alloy clusters within the $As_{20}$ cage exhibit a rich phase space with a large number of low-lying spin states. This is particularly true for clusters with larger number of Mn atoms. The clusters with ferrimagentic spin ordering are found to be more stable compared to those with ferromagnetic ordering. It can be mentioned here that in the pure Mn

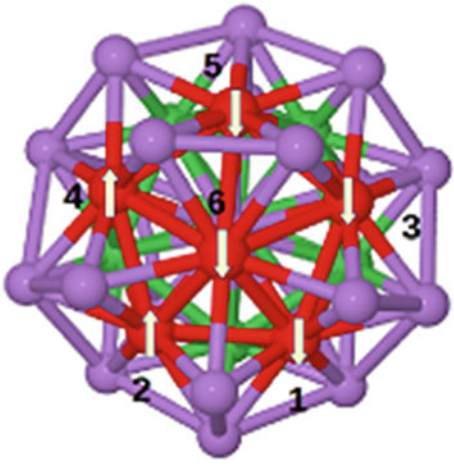


**Fig. 11** Spin ordering of the Mn atoms in the lowest energy spin state of $As@Ni_6Mn_6@As_{20}$

**Table 4** The lowest ferro- and anti-ferromagnetic states of the Mn doped $As@Ni_{12}@As_{20}$ cluster

| Systems | State | MAE (K) | M.M ($\mu_B$) | H–L gap (eV) | ΔE (eV) |
|---|---|---|---|---|---|
| $As_{21}Ni_{11}Mn$ | FM | 10.4 | 6 | 0.07 | 0.0 |
| $As_{21}Ni_{10}Mn_2$ | FM | 20.4 | 9 | 0.25 | 0.0 |
| | AFM | 0.0 | 1 | 0.23 | 0.12 |
| $As_{21}Ni_9Mn_3$ | FM | 37.4 | 12 | 0.33 | 0.15 |
| | AFM | 18.6 | 4 | 0.47 | 0.0 |
| $As_{21}Ni_8Mn_4$ | FM | 32.8 | 15 | 0.16 | 0.18 |
| | AFM | 0.0 | 1 | 0.45 | 0.0 |
| $As_{21}Ni_7Mn_5$ | FM | 17.2 | 14 | 0.22 | 0.03 |
| | AFM | 11.0 | 2 | 0.32 | 0.0 |
| $As_{21}Ni_6Mn_6$ | FM | 7.1 | 15 | 0.25 | 0.29 |
| | AFM | 12.6 | 5 | 0.32 | 0.0 |

clusters also anti-ferromagnetic or ferrimagentic spin ordering is preferred. The spin charges on the Mn atoms range from 2–3 $\mu_B$ in the alloy clusters, which are lower than the spin charge in pure Mn clusters. The doping introduces changes in the environment around the Mn atoms resulting in anisotropy energy.

## 5 Conclusions

The transition metal alloy clusters offer the possibility of tuning their magnetic properties through size, shape, and chemical composition. The magnetic properties show strong variation with cluster size. Reduction in size leads to enhancement of the magnetic moments. Alloying of 3d transition metal atoms with 4d or 4d non-magnetic metals results in larger magnetic moment for the whole cluster. The structure of the cluster is also important in this regard. For example mixed clusters show enhanced magnetization but similar enhancement is not seen in core-shell structures. This field is growing and needs very systematic analysis. The large variability of cluster shape, size, and composition presents vast potential for development novel materials. At the same time, a large amount of effort is required to examine all possible structures. The energetic preference of spin ordering of the systems poses a significant challenge.

For the development of cluster-based materials, precise control over particle growth and composition is required. The salt of $As@Ni_{12}@As_{20}$ is one example of cluster based material with precise structure. Theoretical studies on such clusters with various compositions can help in pinpointing the materials with novel properties, which can be targeted for synthesis. Another advantage of such materials is the clear passivation of the surface metal atoms, which results in higher chemical stability compared to bare gas-phase clusters. Our calculations presented here show that doping with magnetic atoms could lead to enhanced magnetic anisotropy of these clusters. More studies need to be done by varying the composition.

**Acknowledgments** This work was partially supported by DOE Basic Energy Sciences. This work was partially supported by the DOE Basic Energy Science under award numbers DE-SC0006818, and DE-SC0002168 and the NSF PREM program between UCSB and UTEP (DMR-1205302). The authors thank the Texas Advanced Computing Center (TACC) from the National Science Foundation (NSF) (Grant no. TG-DMR090071) and NERSC for the computational time.

## References

1. Néel L (1949) Ann Géophys 5:99
2. Jun YW, Seo JW, Cheon A (2008) Acc Chem Res 41:179
3. Lim EK, Kim T, Paik S, Haam S, Huh YM, Lee K (2015) Chem Rev 115:327
4. Ferrando R, Jellinek J, Johnston RL (2008) Chem Rev 108:845
5. Reddy BV, Khanna SN, Dunlap BI (1993) Phys Rev Lett 70:3323
6. Dunlap BI (1990) Phys Rev A 41:5691
7. Dunlap BI (1991) Z Phys D Atom Mol Cl 19:255
8. Chretien S, Salahub DR (2002) Phys Rev B 66
9. Vega A, Balbas LC, Dorantesdavila J, Pastor GM (1994) Phys Rev B 50:3899
10. Pastor GM, Dorantesdavila J (1995) Phys Rev B 52:13799
11. Alvarado P, Dorantes-Davila J, Pastor GM (1998) Phys Rev B 58:12216
12. Pastor GM (1998) Curr Probl Conden Matter 161
13. Munoz-Navia M, Dorantes-Davila J, Zitoun D, Amiens C, Jaouen N, Rogalev A, Respaud M, Pastor GM (2009) Appl Phys Lett 95
14. Borras-Almenar JJ, Coronado E, Clemente-Juan JM, Palii AV, Tsukerblat BS (2003) Polyhedron 22:2521
15. Jones NO, Beltran MR, Khanna SN, Baruah T, Pederson MR (2004) Phys Rev B 70
16. Jones NO, Khanna SN, Baruah T, Pederson MR (2004) Phys Rev B 70
17. Datta S, Saha-Dasgupta T (2013) J Phys-Condens Mat 25
18. Sahoo S, Islam MF, Khanna SN (2015) New J Phys 17
19. Rohart S, Raufast C, Favre L, Bernstein E, Bonet E, Dupuis V (2006) Phys Rev B 74
20. Luis F, Bartolome J, Bartolome F, Martinez MJ, Garcia LM, Petroff F, Deranlot C, Wilhelm F, Rogalev A (2006) J Appl Phys 99
21. Xie YN, Blackman JA (2006) Phys Rev B 74
22. Bornemann S, Minar J, Staunton JB, Honolka J, Enders A, Kern K, Ebert H (2007) Eur Phys J D 45:529
23. Oda T, Yokoo Y, Sakashita H, Tsujikawa M (2009) J Comput Theor Nanosci 6:2603
24. Boufala K, Fernandez-Seivane L, Ferrer J, Samah M (2010) J Magn Magn Mater 322:3428
25. Islam MF, Khanna SN (2014) J Phys-Condens Mat 26
26. Giguere A, Foldeaki M, Dunlap RA, Chahine R (1999) Phys Rev B 59:431
27. Jamet M, Negrier M, Dupuis V, Tuaillon-Combes J, Melinon P, Perez A, Wernsdorfer W, Barbara B, Baguenard B (2001) J Magn Magn Mater 237:293
28. Kortus J, Baruah T, Pederson MR, Ashman C, Khanna SN (2002) Appl Phys Lett 80:4193
29. Aguilera-Granja F, Vega A (2009) Phys Rev B 79
30. Chen HX, Shi DN, Qi JS, Wang BL (2011) J Magn Magn Mater 323:781
31. Fink K (2006) Chem Phys 326:297
32. Sattler K (1986) Z Phys D Atom Mol Cl 3:223
33. Li SF, Xue XL, Jia Y, Zhao GF, Zhang MF, Gong XG (2006) Phys Rev B 73
34. Mukherjee S, Moranlopez JL (1987) Surf Sci 189:1135
35. Vega A, Dorantesdavila J, Pastor GM, Balbas LC (1991) Z Phys D Atom Mol Cl 19:263
36. Sumiyama K, Suzuki K, Makhlouf SA, Wakoh K, Kamiyama T, Yamamuro S, Konno TJ, Xu YF, Sakurai M, Hihara T (1995) J Non-Cryst Solids 193:539

37. Manago T, Otani Y, Miyajima H, Akiba E (1996) J Appl Phys 79:5126
38. Brayner R, Coradin T, Fievet-Vincent F, Livage J, Fievet F (2005) New J Chem 29:681
39. Zitoun D, Respaud M, Fromen M-C, Casanove MJ, Lecante P, Amiens C, Chaudret B (2002) Phys Rev Lett 89:037203
40. Dennler S, Morillo J, Pastor GM (2004) J Phys-Condens Mat 16:S2263
41. Munoz-Navia M, Dorantes-Davila J, Pastor GM (2004) J Phys-Condens Mat 16:S2251
42. Tournus F, Blanc N, Tamion A, Hillenkamp M, Dupuis V (2010) Phys Rev B 81
43. Muñoz-Navia M, Dorantes-Dávila J, Respaud M, Pastor GM (2009) Eur Phys J D 52:171
44. Blanc N, Diaz-Sanchez LE, Ramos AY, Tournus F, Tolentino HCN, De Santis M, Proux O, Tamion A, Tuaillon-Combes J, Bardotti L, Boisron O, Pastor GM, Dupuis V (2013) Phys Rev B 87
45. Guirado-Lopez R, Villasenor-Gonzalez P, Dorantes-Davila J, Pastor GM (2003) Eur Phys J D 24:73
46. Sahoo S, Hucht A, Gruner ME, Rollmann G, Entel P, Postnikov A, Ferrer J, Fernandez-Seivane L, Richter M, Fritsch D, Sil S (2010) Phys Rev B 82
47. Liebing S, Martin C, Trepte K, Kortus J (2015) Phys Rev B 91
48. Pederson MR, Khanna SN (1999) Phys Rev B 60:9566
49. Blonski P, Hafner JJ (2011) Phys-Condens Mat 23
50. Pederson MR, Baruah T (2007) Molecular magnets: phenomenology and theory, chapter 9 in handbook of magnetism and advanced magnetic materials. Wiley, Hoboken
51. Pederson MR, Jackson KA (1990) Phys Rev B 41:7453
52. Jackson K, Pederson MR, Erwin SC (1990) Forces and geometry optimization in 1st-principles atomic cluster calculations, vol 193
53. Jackson K, Pederson MR (1990) Phys Rev B 42:3276
54. Pederson MR, Klein BM, Broughton JQ (1988) Phys Rev B 38:3825
55. Pederson MR, Porezag DV, Kortus J, Patton DC (2000) Phys Status Solidi B-Basic Res 217:197
56. Pederson MR, Baruah T, Allen PB, Schmidt C (2005) J Chem Theory Comput 1:590
57. Pederson MR, Khanna SN (1999) Chem Phys Lett 307:253
58. Pederson MR, Bernstein N, Kortus J (2002) Phys Rev Lett 89
59. Kortus J, Baruah T, Bernstein N, Pederson MR (2002) Phys Rev B 66
60. Kortus J, Pederson MR, Hellberg CS, Khanna SN (2001) Eur Phys J D 16:177
61. Baruah T, Kortus J, Pederson MR, Wesolowski R, Haraldsen JT, Musfeldt JL, North JM, Zipse D, Dalal NS (2004) Phys Rev B 70
62. Pederson MR, Kortus J, Khanna SN (2002) J Appl Phys 91:7149
63. Park K, Pederson MR, Richardson SL, Aliaga-Alcalde N, Christou G (2003) Phys Rev B 68
64. Baruah T, Pederson MR (2002) Chem Phys Lett 360:144
65. Piligkos S, Rajaraman G, Soler M, Kirchner N, van Slageren J, Bircher R, Parsons S, Gudel HU, Kortus J, Wernsdorfer W, Christou G, Brechin EK (2005) J Am Chem Soc 127:5572
66. Baruah T, Pederson MR (2002) Chem Phys Lett 360:144
67. Kortus J, Pederson MR, Baruah T, Bernstein N, Hellberg CS (1871) Polyhedron 2003:22
68. Gambardella P, Rusponi S, Veronese M, Dhesi SS, Grazioli C, Dallmeyer AIC, Zeller R, Dederichs PH, Kern K, Carbone C, Brune H (2003) Science 300:1130
69. Xiao RJ, Fritsch D, Kuz'min M D, Koepernik K, Eschrig H, Richter M, Vietze K, Seifert G (2009) Phys Rev Lett 103
70. Fritsch D, Koepernik K, Richter M, ESchrig H (2008) J Comput Chemis 29:2210
71. Strandberg TO, Canali CM, MacDonald AH (2008) Phys Rev B 77
72. Garcia-FuenteA, Vega A, Aguilera-Granja F, Gallego L (2009) J Phys Rev B 79
73. Garcia-Fuente A, Garcia-Suarez VM, Ferrer J, Vega A (2012) Phys Rev B 85
74. Moses MJ, Eichhorn B, Fettinger J (2003) Abstracts Papers Am Chem Soc 225:U85
75. Baruah T, Zope RR, Richardson SL, Pederson MR (2004) J Chem Phys 121:11007
76. Baruah T, Zope RR, Richardson SL, Pederson MR (2003) Phys Rev B 68